Wireless Power Transfer

ARTICLE

Open Access

https://doi.org/10.48130/wpt-0026-0001

Wireless Power Transfer **2026**, 13: e011

Research on constant voltage and constant current dual-load wireless power transfer system based on composite control method

Haibing Wang[1,2], Yao Dong[3], Zhiyuan Peng[2], Yu Cai[2], Shaobo Ma[2], Jianjun Hu[1] and Lu Zhang[3*]

[1] *The State Key Laboratory of Mechanical Transmission for Advanced Equipment, Chongqing University, Chongqing 400044, China*
[2] *Chongqing Tsingshan industrial Co., Ltd. Chongqing 402776, China*
[3] *School of Electrical and Electronic Engineering, Chongqing University of Technology, Chongqing 400054, China*
* Correspondence: road@cqut.edu.cn (Zhang L)

Abstract

Existing wireless power transfer (WPT) systems often fail to simultaneously achieve constant-voltage (CV) and constant-current (CC) outputs when charging multiple devices. To address this limitation, this paper proposes a dual-load WPT system with CV and CC characteristics. The system comprises a full-bridge rectifier circuit for CC output and a novel half-wave rectifier circuit for CV output, along with a composite CV/CC control method to independently regulate power across the two output circuits. First, the power transfer characteristics of the proposed circuit topology are analyzed, and the operational principles of the novel half-wave rectifier are elucidated. Second, a transfer function model of the dual-load WPT system is established, and the composite CV/CC control strategy is introduced: feedforward PI control with phase-shift voltage regulation enables CC output for the full-bridge rectifier circuit, while PI control ensures CV output for the half-wave rectifier circuit. Finally, an experimental prototype is constructed to validate the power transfer characteristics and the composite CV/CC control method. Experimental results demonstrate the feasibility and stability of the proposed approach.

Citation: Wang H, Dong Y, Peng Z, Cai Y, Ma S, et al. 2026. Research on constant voltage and constant current dual-load wireless power transfer system based on composite control method. *Wireless Power Transfer* 13: e011 https://doi.org/10.48130/wpt-0026-0001

Introduction

Wireless power transfer (WPT) technology overcomes the safety hazards associated with traditional wired power supply, offering advantages such as environmental sustainability, safety, and flexibility. It has been widely adopted in fields including electric vehicles, underwater equipment, and implantable medical devices[1–6]. In recent years, with the expansion of application scenarios, multi-load WPT technology has garnered increasing attention. Compared to single-load WPT systems, multi-load systems exhibit superior load capacity, greater spatial flexibility at the load end, and higher power density. Based on the number of transmitter coils, multi-load WPT systems are primarily categorized into 'single-to-multiple' and 'multiple-to-multiple' power supply modes.

In the 'single-to-multiple' power supply mode, the optimal load reactance was derived to compensate for coil cross-coupling, with experimental validation on dual-load and triple-load systems[7]. To address output power instability caused by mutual inductance variations, a DC-DC converter-based power distribution method that maintains constant total output power was proposed[8]. Relay coils enabled multi-load constant-voltage power delivery, although relay-induced losses compromised system efficiency[9]. Finally, 92% efficiency was achieved in a 100 W multi-load WPT system through optimized coil design that ensured constant transmitter coil current and load position insensitivity[10].

For the 'multiple-to-multiple' power supply mode, a multi-phase coil structure and multi-frequency phase-shift control strategy were proposed to achieve power distribution and enhance misalignment tolerance, though the parallel-inverter configuration increased system complexity[11]. To simplify control and eliminate additional power converters at loads, a hybrid compensation topology was utilized to establish independent power-frequency channels with minimal inter-channel interference[12]. An omnidirectional transmitter coil was developed to enable uniform efficiency transmission across multiple loads through a rotational magnetic field generated by phase-shifted currents[13].

Moreover, closed-loop feedback control is essential to achieve precise and stable output power under external disturbances such as load variations and input voltage fluctuations in WPT systems. Genetic algorithm (GA)-optimized PID control was implemented for parameter tuning, though its dependence on initial parameter settings presents implementation challenges[14]. For series-compensated WPT systems, a discrete sliding mode control method was developed, enabling simultaneous maximum efficiency tracking and output voltage regulation[15]. A hybrid one-cycle control with proportional-derivative compensation (OCC-PD) ensured fast transient response, although the complex control strategy complicates mathematical modeling across different topologies[16].

Therefore, both single-to-multiple and multiple-to-multiple multi-load WPT systems exhibit two critical limitations:

First, cross-coupling between transmitter and receiver coils reduces power transfer efficiency. While dedicated decoupling coils can partially mitigate this issue, their strict load-quantity constraints limit practical applications beyond systems with few loads.

Second, achieving independent power regulation across output channels is inherently difficult. Although natural resonance conditions in hybrid compensation topologies support CV/CC outputs[17–19], the voltage and current at each load remain rigidly fixed by system parameters. This leads to significant output power degradation during external disturbances such as input voltage fluctuations or extreme load variations.

To further improve the transmission performance of WPT systems, achieve constant outputs for different channels, and enhance output stability, this paper proposes a control method for constant voltage-constant current (CV/CC) output and independent power regulation in a dual-load WPT system. A dual-load WPT system

integrated with two types of rectifier circuits (a full-wave rectifier circuit and a half-wave rectifier circuit) is designed. This system can successfully realize independent power regulation for the two output channels and is capable of supplying power to energy storage systems and loads that require positive-negative polarity switching.

A mathematical model of the LCC-LCC multi-load WPT system is established, and the transmission characteristics of the two output channels are analyzed in detail. On this basis, a composite constant voltage and constant current (CV/CC) output control strategy is introduced: a feedforward PI control is adopted at the transmitter to achieve constant current output of the full-wave rectifier circuit, and a PI control is applied at the receiver to maintain constant voltage output of the half-wave rectifier circuit, thereby realizing the independent regulation of output power. This method ensures the decoupled operation of the two control loops, enabling the system to maintain CV/CC outputs and independent power regulation when subjected to disturbances.

System configuration and transmission characteristics analysis

System structure

As shown in Fig. 1, the proposed LCC-LCC compensated dual-load WPT system employs a full-bridge inverter using power switches S_1–S_4 to drive the power conversion stage. The transmitter LCC compensation network consists of compensation inductor L_{f1} with capacitors C_{f1} and C_P, while the receiver LCC network incorporates inductor L_{f2} with capacitors C_{f2} and C_S. Transmitter coil L_P and load coil L_S are magnetically coupled through mutual inductance M. Output regulation utilizes two distinct rectification paths: diodes D_1–D_4 form a full-bridge rectifier for #A output circuit, whereas power switches S_P and S_n constitute a half-wave active rectifier for #B output circuit. Filter capacitors C_1 and C_2 smooth the outputs for channels #A and #B, respectively. R_{f1}, R_P, R_S, and R_{f2} are the internal resistances of L_{f1}, L_P, L_S, and L_{f2}, respectively, while R_a and R_b form the output loads of the two circuits.

For the #A output circuit, the constant current output can be achieved by utilizing the characteristics of the LCC-LCC compensation topology. In the #B output circuit, the positive half-wave rectifier outputs a forward voltage by controlling switch S_P, while the negative half-wave rectifier outputs a reverse voltage by controlling switch S_n.

Analysis of transmission performance in LCC-LCC dual-load WPT systems

Compared to conventional multi-load WPT systems operating in 'single-to-multiple' or 'multiple-to-multiple' power delivery modes, the circuit configuration in Fig. 2 eliminates multi-coil coupling by adopting a single-to-single power transfer architecture. Specifically, this topology employs only one transmitter and one receiver, thereby eliminating undesirable cross-coupling effects between multiple coils on output power regulation.

Here, U_{in} denotes the inverter output voltage. To simplify analysis, the theoretical derivation employs the fundamental harmonic approximation (FHA) method. By controlling the inverter through phase-shifted modulation (PSM), the fundamental component of the inverter output voltage can be expressed in phasor form as:

$$U_{in} = \frac{2\sqrt{2}V_{dc}}{\pi}\sin\frac{\delta}{2}\angle 0^\circ \tag{1}$$

Where δ is the phase-shift angle of the inverter.

Applying Kirchhoff's Voltage Law (KVL) to the equivalent model shown in Fig. 2:

$$\begin{bmatrix} U_{in} \\ 0 \\ 0 \\ 0 \end{bmatrix} = \begin{bmatrix} R_{f1}+j\omega L_{f1}+\frac{1}{j\omega C_{f1}} & -\frac{1}{j\omega C_{f1}} & 0 & 0 \\ -\frac{1}{j\omega C_{f1}} & R_P+j\omega L_P+\frac{1}{j\omega C_P}+\frac{1}{j\omega C_{f1}} & -j\omega M & 0 \\ 0 & -j\omega M & R_S+j\omega L_S+\frac{1}{j\omega C_S}+\frac{1}{j\omega C_{f2}} & -\frac{1}{j\omega C_{f2}} \\ 0 & 0 & -\frac{1}{j\omega C_{f2}} & R_L+R_{f2}+j\omega L_{f2}+\frac{1}{j\omega C_{f2}} \end{bmatrix} \cdot \begin{bmatrix} I_{in} \\ I_P \\ I_S \\ I_o \end{bmatrix} \tag{2}$$

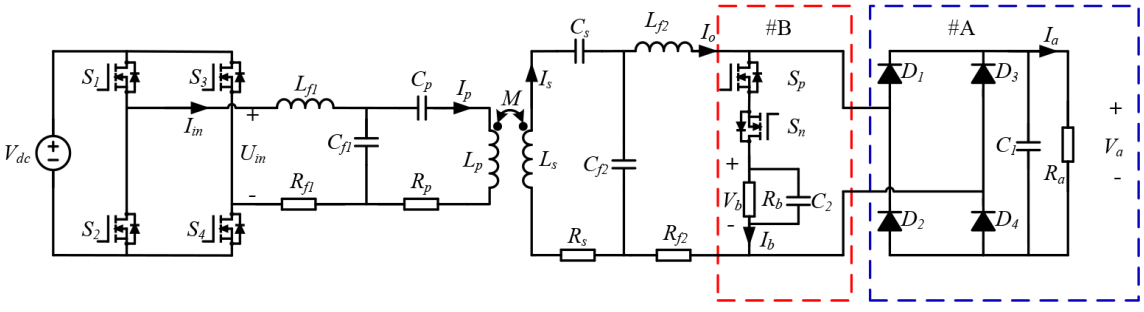

Fig. 1 Topology of the dual-load WPT system with constant-voltage and constant-current capabilities.

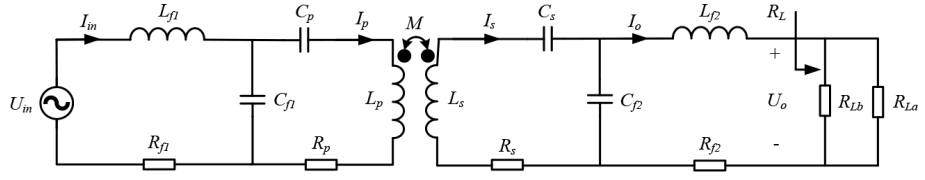

Fig. 2 Equivalent circuit model.

where, $R_L = R_{La}//R_{Lb}$, R_{La} and R_{Lb} represent the equivalent input impedances of #A output circuit and #B output circuit, respectively, satisfying:

$$R_{La} = \frac{8}{\pi^2}R_a, R_{Lb} = \frac{U_0^2}{V_b^2}R_b \tag{3}$$

where, U_o denotes the voltage across equivalent load R_L, and V_b represents the output voltage of the half-wave rectifier circuit.

To maintain system resonance and reduce reactive power losses, both transmitter and receiver must operate at resonance, with the system angular frequency ω_S matching the inverter operating frequency ω. The resonant components must satisfy:

$$\begin{cases} j\omega L_{f1} + \dfrac{1}{j\omega C_{f1}} = 0 \\ j\omega L_P + \dfrac{1}{j\omega C_P} + \dfrac{1}{j\omega C_{f1}} = 0 \\ j\omega L_S + \dfrac{1}{j\omega C_S} + \dfrac{1}{j\omega C_{f2}} = 0 \\ j\omega L_{f2} + \dfrac{1}{j\omega C_{f2}} = 0 \end{cases} \tag{4}$$

Substituting Eq. (4) into Eq. (2) yields the expressions for the currents in each loop:

$$\begin{cases} I_{in} = \dfrac{U_{in}}{Z_{in}} \\ I_p = \dfrac{-j\omega L_{f1}(\omega^2 {L_{f2}}^2 + R_L R_S + R_S R_{f2})}{\omega^2({L_{f2}}^2 R_P + M^2 R_L + M^2 R_{f2}) + R_P R_S (R_L + R_{f2})} I_{in} \\ I_S = \dfrac{\omega^2 M L_{f1}(R_L + R_{f2})}{\omega^2({L_{f2}}^2 R_P + M^2 R_L + M^2 R_{f2}) + R_P R_S (R_L + R_{f2})} I_{in} \\ I_o = \dfrac{j\omega^3 M L_{f1} L_{f2}}{\omega^2({L_{f2}}^2 R_P + M^2 R_L + M^2 R_{f2}) + R_P R_S (R_L + R_{f2})} I_{in} \end{cases} \tag{5}$$

According to Eq. (5), the equivalent input impedance of the dual-load WPT system can be obtained as:

$$Z_{in} = R_{f1} + \frac{\omega^2 {L_{f1}}^2 R_S (R_L + R_{f2}) + \omega^4 {L_{f1}}^2 {L_{f2}}^2}{(R_P R_S + \omega^2 M^2)(R_L + R_{f2}) + \omega^2 {L_{f2}}^2 R_P} \tag{6}$$

And the expression for the equivalent voltage U_o at the load side after passing through the compensation network can be derived as:

$$U_o = \frac{j\omega^3 M L_{f1} L_{f2} R_L}{\omega^2({L_{f2}}^2 R_P + M^2 R_L + M^2 R_{f2}) + R_P R_S (R_L + R_{f2})} I_{in} \tag{7}$$

According to Eq. (5), the expressions for the output power and transmission efficiency of the equivalent load R_L can be derived as:

$$\begin{cases} P_o = \dfrac{e\omega^2 M^2 U_{in}^2 R_L}{[aR_{f1} + \omega^2(bR_{f1} + cR_{f1} + d) + e]^2} \\ \eta = \dfrac{e\omega^2 M^2 R_L}{(a + \omega^2(b + c))(aR_{f1} + \omega^2(bR_{f1} + cR_{f1} + d) + e)} \end{cases} \tag{8}$$

where, parameters *a*–*e* are defined as:

$$\begin{cases} a = R_P R_S (R_L + R_{f2}) \\ b = M^2 (R_L + R_{f2}) \\ c = L_{f2}^2 R_P \\ d = L_{f1}^2 R_S (R_L + R_{f2}) \\ e = \omega^4 L_{f1}^2 L_{f2}^2 \end{cases} \tag{9}$$

For #A output circuit, the voltage gain of the full-bridge rectifier is given by:

$$I_a = \frac{V_a}{R_a} = \frac{\sqrt{2}\pi U_o}{4R_a} \tag{10}$$

Analysis of half-wave rectifier circuit

Compared to the #A output circuit, the #B output circuit employs two anti-series power switches (S_P and S_n) forming a half-wave rectifier. This topology enables bidirectional voltage regulation to meet load polarity requirements. Figure 3 illustrates the operational modes of Output #B.

Mode 1: Forward conduction mode

In this mode, the positive half-wave rectifier operates. The power switch S_n is turned off, and the body diode anti-parallel to switches S_p and S_n forms a forward conduction path. The output current I_b of the #B output circuit is positive, providing a forward output voltage for the load. This is shown in Fig. 3a.

Mode 2: Reverse conduction mode

In this mode, the negative half-wave rectifier operates. Switch S_p is turned off, and the body diodes anti-parallel to S_n and S_p form a reverse conduction path. The output current I_b of the #B output circuit is negative, enabling it to provide a reverse output voltage for the load. The schematic diagram is shown in Fig. 3b.

As can be seen from Fig. 3, since two half-wave rectifiers are integrated into one channel, the polarity switching of the load output voltage can be achieved simply by controlling the turn-on and turn-off of two anti-parallel power switching devices. Meanwhile, the designed response control method is more concise, which will be explained in the next section.

The output voltage of the positive half-wave rectifier in #B output circuit is given by:

$$V_b = \frac{1}{2\pi}\int_0^{2\pi D_{sp}} \sqrt{2}U_o \sin(\omega t) d\omega t = \frac{\sqrt{2}U_o}{2\pi}\left(1 - \cos\left(2\pi D_{sp}\right)\right) \tag{11}$$

where, D_{sp} is the duty cycle of switch S_P's drive signal during the positive half-cycle. Similarly, the output voltage of the negative half-wave rectifier in #B output circuit is expressed as:

$$-V_b = -\frac{1}{2\pi}\int_{\pi}^{\pi+2\pi D_{sp}} \sqrt{2}U_o \sin(\omega t) d\omega t = \frac{\sqrt{2}U_o}{2\pi}\left(1 - \cos\left(2\pi D_{sp}\right)\right) \tag{12}$$

From the above analysis, it can be concluded that the #A output circuit can maintain a constant current I_a by virtue of the characteristics of the LCC-LCC compensation network. For the output #B, a stable output voltage V_b can be achieved by determining the switching frequency and duty cycle of the control switches S_p and S_n.

Composite constant voltage and current output control strategy

As derived from Eqs (10), (11), and (12), the output current I_a of the output #A and the output voltage V_b of the #B output circuit can be regulated independently.

By substituting Eqs (1), (5), and (10) into Eq. (15) while neglecting the coil resistance, the inverter output voltage, equivalent load R_{La} of the output #A, ac-side current I_o, and full-wave rectifier output current I_a in the dual-load WPT system can be reformulated as:

$$\begin{cases} U_{in} = \dfrac{2\sqrt{2}}{\pi} V_{dc} \sin\dfrac{\delta}{2} \\ I_o = \left|\dfrac{MU_{in}}{\omega L_{f1} L_{f1}}\right| \\ I_a = \dfrac{\sqrt{2}\pi I_o R_{La}}{4R_a} \end{cases} \tag{13}$$

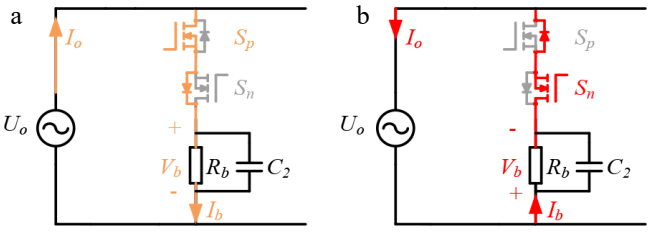

Fig. 3 Equivalent circuit of #B output circuit. (a) Forward conduction mode. (b) Reverse conduction mode.

The expression for the inverter phase-shift angle δ can be derived as:

$$\delta = 2\arcsin\left(\frac{\pi^2\omega L_{f1}L_{f2}I_a}{8MV_{dc}}\right) \tag{14}$$

To achieve constant-current output for #A output circuit and constant-voltage output for #B output circuit with independent power control, it is essential to enhance the system's disturbance rejection capability. Therefore, selecting an appropriate control strategy is crucial. This section focuses on improving the constant current control performance of #A output circuit by combining feedforward PI control with phase-shift modulation, while #B output circuit employs conventional PI control for constant-voltage regulation.

Design of feedforward PI controller

In the dual-load WPT system, the presence of delays and errors in PI control can reduce the system's control tracking performance. To address this issue, a feedforward controller is introduced to improve the system's response speed and control accuracy. Its core idea is to reduce output deviations by predicting and compensating for changes in external disturbances or system inputs in advance. PI control can compensate for system errors and disturbances, while feedforward control can predict the system's output in advance and perform compensation simultaneously. Through the combined action of PI control and the feedforward link, high-precision constant current output control of the dual-load WPT system can be achieved.

Figure 4 illustrates the control schematic combining PI control with feedforward compensation. In this diagram, $R(s)$ and $Y(S)$ represent the input and output variables, respectively, $G_f(S)$ denotes the transfer function of the feedforward controller, $K_p + K_i/S$ corresponds to the transfer function of the PI controller, and $G_p(S)$ describes the transfer function of the controlled plant. The error signal $E(S)$ is defined as $E(S) = R(S) - Y(S)$.

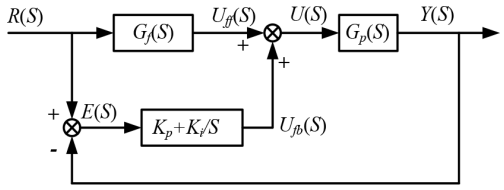

Fig. 4 Schematic diagram of feedforward PI control.

From Fig. 4, the transfer function of the feedforward control can be derived as:

$$U_{ff}(S) = G_f(S)R(S) \tag{15}$$

Similarly, the transfer function of the PI control can be obtained as:

$$U_{fb}(S) = \left(K_p + \frac{K_i}{S}\right)E(S) \tag{16}$$

By superimposing the feedforward and PI control loop equations shown in Eqs (15) and (16), the total control output can be expressed as:

$$U(S) = U_{ff}(S) + U_{fb}(S) \tag{17}$$

Based on the aforementioned theoretical analysis, the closed-loop output expression can be derived as:

$$Y(S) = \frac{G_p(S)\left[G_f(S) + \left(K_p + \frac{K_i}{S}\right)\right]R(S)}{1 + G_p(S)\left(K_p + \frac{K_i}{S}\right)} \tag{18}$$

In Eq. (18), the feedforward path $G_f(S)$ enables direct generation of control actions from the reference input $R(S)$, achieving rapid command tracking through immediate response to input variations. Simultaneously, the error signal $E(S)$ facilitates adaptive control adjustment to suppress disturbances and eliminate steady-state errors. The synergistic integration of feedforward and PI control enhances the system's dynamic response speed while ensuring robust performance and improved disturbance rejection capability.

For #B output circuit, constant-voltage output can be achieved by implementing real-time detection of the voltage U_o across the receiver equivalent load R_L, followed by PI control regulation according to Eqs (11) and (12).

The overall control block diagram proposed in this paper is shown in Fig. 5.

In Fig. 5, for #A output circuit, the measured output current I_a is acquired through the current sensing circuit and the A/D conversion module. This signal is then processed by the feedforward compensation block before being compared with the reference current I_{af}. The resulting error signal is fed into the PI controller, whose output is transmitted to the phase-shift modulation module for conduction angle calculation. This modulated signal ultimately drives the full-bridge inverter circuit to regulate I_o, thereby controlling the output current I_a.

For #B output circuit, the load voltage V_b across R_b is measured and compared with the reference voltage V_{bf} (or $-V_{bf}$). The resulting

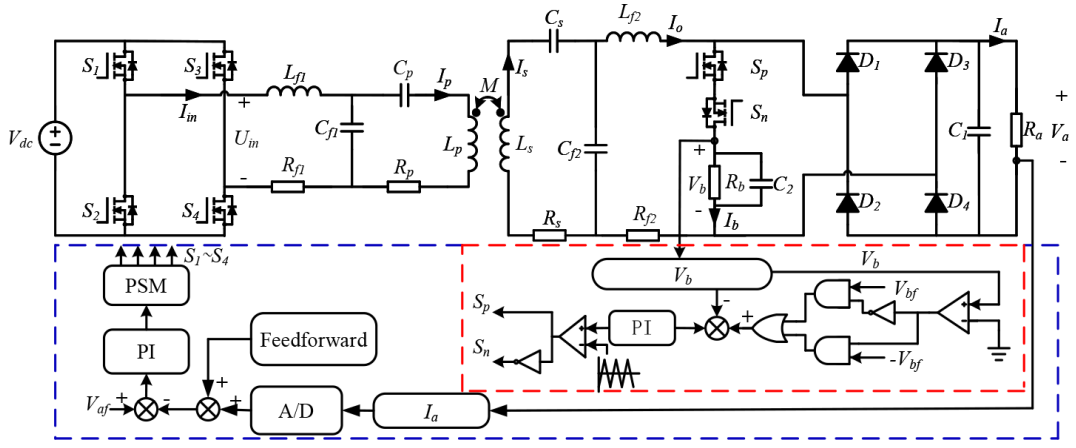

Fig. 5 Schematic diagram of the composite control strategy for dual-load WPT systems.

error signal is processed by the PI controller, which regulates the switching operations of D_{sp} and D_{sn} to adjust V_b. This control methodology enables independent multi-channel power output while maintaining excellent system stability.

Based on the above analysis, the design flowchart of system parameters is illustrated in Fig. 6.

Experimental verification

Experimental platform

To validate the feasibility of the proposed composite constant-voltage and current control method for the dual-load WPT system, an experimental prototype was constructed as shown in Fig. 7.

The entire system consists of a high-frequency inverter, an LCC-LCC compensation circuit, transmitting and receiving coils, a half-wave rectifier, a full-bridge rectifier, loads, and a control circuit, with the system resonance frequency set to 85 KHz. To ensure the generation of high-frequency power, gallium nitride (GaN) power switching devices with high switching frequency and low switching loss are used to form the high-frequency inverter circuit and the half-wave rectifier circuit. The control algorithm is implemented using the TMS320F28335 DSP from TI. Table 1 presents the specific experimental parameters of the system.

ZVS verification

The composite CV/CC control method proposed in this paper is implemented by phase-shift voltage regulation using the inverter at the transmitter. Through the built experimental platform, under the condition that $R_a = R_b = 10\ \Omega$ and with different reference output currents I_a and output voltages V_b, the waveforms of the inverter output voltage U_{in} and output current I_{in} at the transmitter are shown in Fig. 8. As can be seen, when the system output reference value changes, tracking of the output reference value can be achieved by adjusting the phase-shift angle of the inverter, and the system can realize Zero Voltage Switching (ZVS).

Analysis on the control effect of composite constant voltage and current

This paper proposes a composite CV/CC control method that can maintain the output current I_a of Circuit #A and the output voltage V_b of Circuit #B constant. Notably, for V_b, positive and negative polarity switching can be performed according to load requirements. Therefore, studying the effect of composite CV/CC control is of great necessity, which can be specifically divided into two parts: first, verifying whether I_a and V_b can be independently controlled, that is, whether the output power of Circuits #A and #B can realize independent power regulation; second, verifying whether the amplitude of V_b remains consistent after polarity switching, that is, the magnitude of the output power remains unchanged before and after polarity switching, and only the power direction changes.

Figure 9 shows the waveforms when the reference value of the output current I_a remains unchanged while the reference value of the output voltage V_b changes. As can be seen from the figure, I_a always remains at the set reference value, and at the same time, V_b can also track different reference output voltages.

Fixing the output voltage of V_b at ±15 V, the experimental waveforms when the reference value of I_a's output is changed are shown in Fig. 10. It can be seen that no matter how the reference current of I_a changes, it does not affect the output of V_b, which verifies that the output power of Circuits #A and #B can achieve independent control, with almost no mutual influence between them.

By combining the experimental waveforms of I_a and V_b shown in Figs 9 and 10, the effect of the composite CV/CC control method can be verified. Furthermore, through a comprehensive comparison of the experimental waveforms in the two figures, it can be seen that for V_b, whether it is switching from positive polarity voltage to negative polarity voltage or from negative polarity voltage to positive polarity voltage, its amplitude remains consistent before and after polarity switching. This further proves that the system's output power is not affected by polarity switching.

The measured system transmission efficiency before and after the polarity switching points is shown in Fig. 11. As can be seen, when R_a and R_b vary within a certain range, the system transmission efficiency remains at a high level overall, which indirectly indicates that

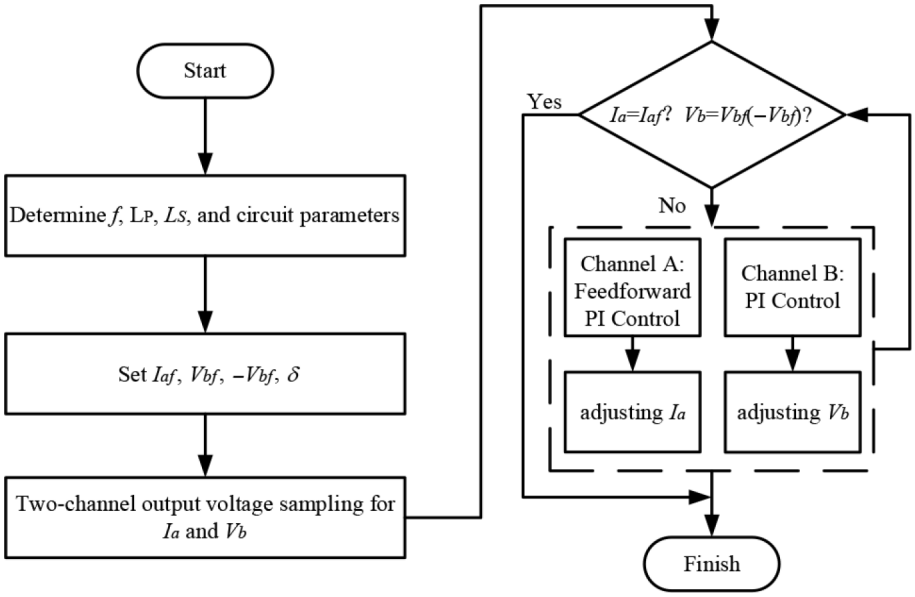

Fig. 6 System operation flowchart.

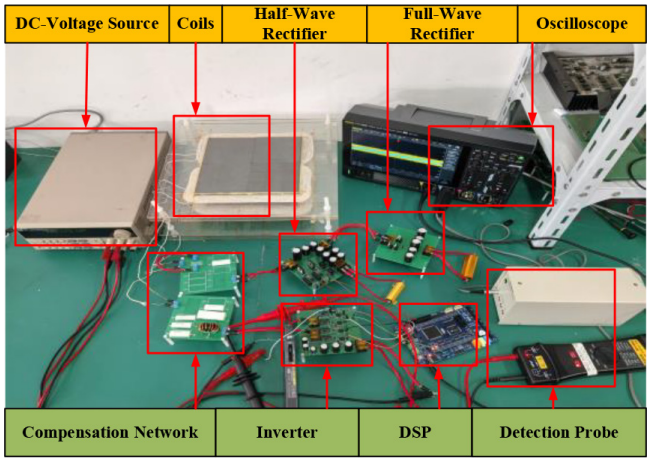

Fig. 7 Experimental platform.

Table 1. Experimental parameters.

Item	Value	Item	Value
V_{dc}	30 V	f	85 KHz
L_P	247.40 μH	C_P	16.16 nF
L_S	110.69 μH	C_S	45.13 nF
L_{f1}	30 μH	C_{f1}	116.86 nF
L_{f2}	33 μH	C_{f2}	106.24 nF
R_P	0.2 Ω	R_{f1}	0.07 Ω
R_S	0.14 Ω	R_{f2}	0.09 Ω

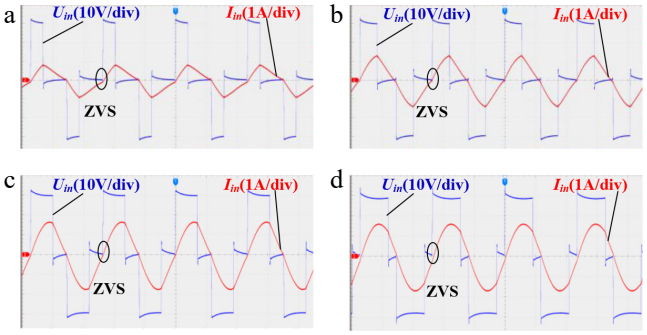

Fig. 8 Waveforms of the inverter's output voltage and current under different reference values. (a) I_a = 1 A,V_b = ±5 V. (b) I_a = 1.2 A,V_b = ±10 V. (c) I_a = 2 A,V_b = ±15 V. (d) I_a = 2.4 A,V_b = ±25 V.

the system transmission efficiency is not affected by the polarity switching of V_b.

Dynamic performance

To study the dynamic performance of the system, with the output reference values at R_a = R_b = 10 Ω (I_a = 1.6 A and V_b = ±10 V) still used as the reference, Fig. 12 shows the dynamic response diagrams when R_a and R_b change, respectively. Figure 12a–c indicate that when R_a changes from 10 Ω→5 Ω→10 Ω, 10 Ω→20 Ω→10 Ω, and 20 Ω→10 Ω→20 Ω, both I_a and V_b can reach the set reference values. The system only has slight fluctuations when the load changes, and polarity switching of V_b at different times does not impact the amplitude of V_b. Figure 12d–f demonstrate that when R_b changes from 10 Ω→5 Ω→10 Ω, 10 Ω→20 Ω→10 Ω, and 20 Ω→10 Ω→20 Ω, the composite CV/CC control method can maintain I_a and V_b constant. The system has no obvious overshoot and can adapt to load variation scenarios.

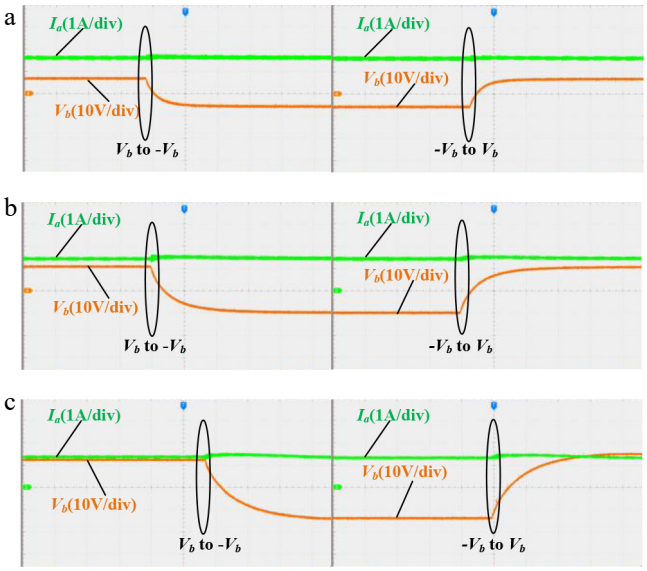

Fig. 9 Verification waveforms of independent power regulation. (a) I_a = 1.6 A,V_b = ±7.5 V. (b) I_a = 1.6 A, V_b = ±10 V. (c) I_a = 1.6 A,V_b = ±15 V.

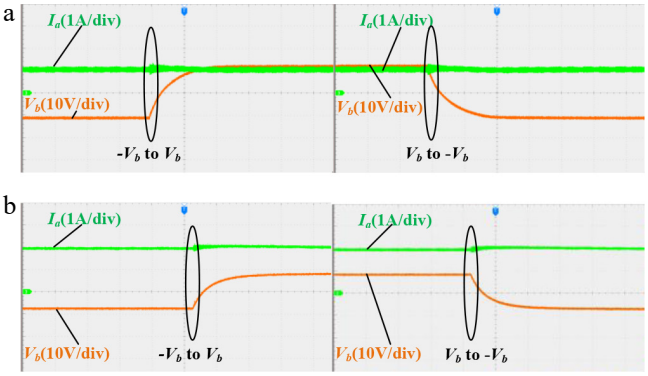

Fig. 10 Experimental waveforms of V_b polarity switching. (a) I_a = 1.2 A,V_b = ±10 V. (b) I_a = 2 A,V_b = ±10 V.

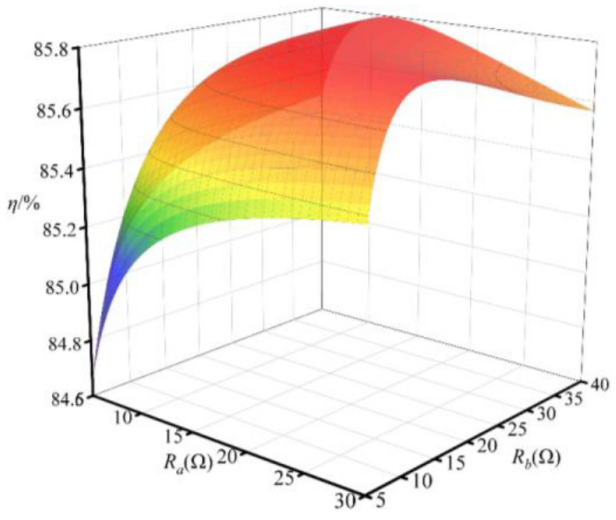

Fig. 11 System transmission efficiency.

Discussion

The composite CV/CC control method proposed in this paper can provide dual-load WPT systems with stable output voltage and

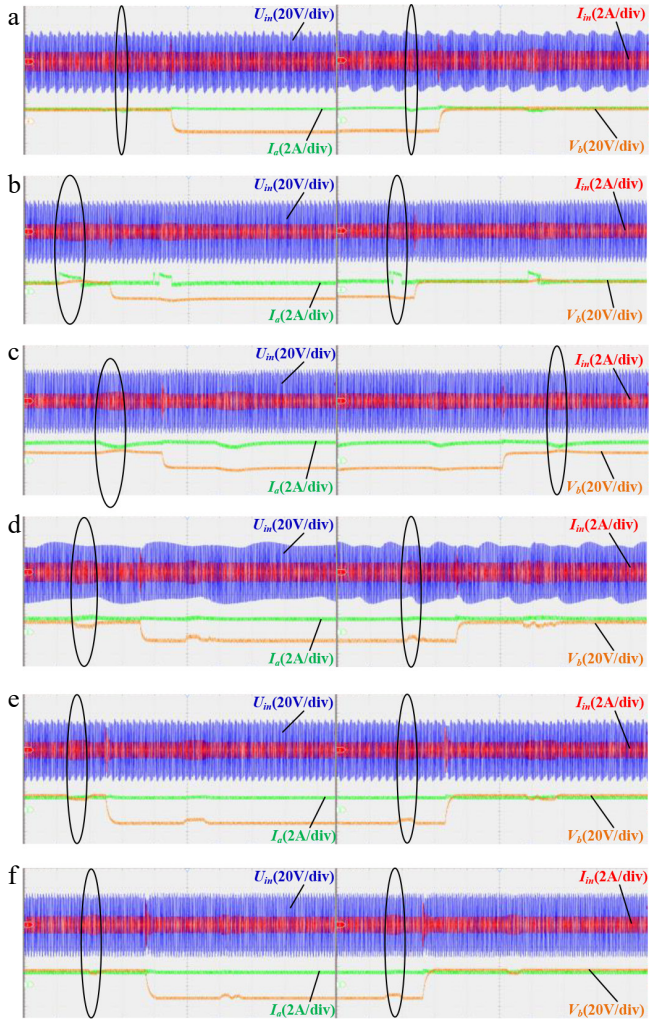

Fig. 12 Dynamic response of the system. (a) R_a: 10 Ω→5 Ω→10 Ω. (b) R_a: 10 Ω→20 Ω→10 Ω. (c) R_a: 20 Ω→10 Ω→20 Ω. (d) R_b: 10 Ω→5 Ω→10 Ω. (e) R_b: 10 Ω→20 Ω→10 Ω. (f) R_b: 20 Ω→10 Ω→20 Ω.

output current. The two output controllers operate in a decoupled manner, and their output powers can be independently adjusted. Notably, a novel half-wave rectifier is designed, which can supply power to loads requiring voltage polarity switching and features convenience and cost-effectiveness. This work provides a new approach to addressing relevant issues in multi-load WPT systems.

Conclusions

To address the challenges of cross-coupling interference between coils and independent power regulation in conventional multi-load WPT systems, this paper proposes an innovative half-wave rectifier capable of output voltage polarity reversal and develops a composite constant-voltage and current control method for dual-output independent power regulation. The proposed solution offers a novel approach to resolving power control limitations in multi-load WPT systems, with the following key advancements:

(1) Proposes a novel active half-wave rectifier that achieves programmable output voltage polarity switching by controlling the switching states of two anti-series power semiconductor devices. The operational principles and control methodology for this rectifier topology are comprehensively established.

(2) A composite constant-voltage and current output control method is proposed. Feedforward PI control is adopted for phase-shift voltage regulation to adjust the inverter output voltage, thereby controlling a constant-current output. With the equivalent load voltage at the receiving end as the carrier, another constant-voltage output is realized through PI control.

It is worth mentioning that the composite CV/CC control method proposed in this paper still requires two controllers. Future research can further consider optimizing the control scheme, where regulation of output voltage and current can be achieved by only applying a controller at the transmitter.

Author contributions

The authors confirm their contributions to the paper as follows: study conception and design: Dong Y; data collection: Wang H, Zhang L, Ma S; analysis and interpretation of results: Peng Z, Cai Y, Hu J; draft manuscript preparation: Wang H, Dong Y. All authors reviewed the results and approved the final version of the manuscript.

Data availability

The datasets generated during the current study are available from the corresponding author upon reasonable request.

Acknowledgments

This research was partially supported by the General Project of Chongqing Natural Science Foundation (Grant No. CSTB2024NSCQ-MSX0382), the Science and Technology Research Project of Chongqing Municipal Education Commission (Grant No. KJQN202201103), and the Joint-funded Project of Chongqing University of Technology (Grant Nos gzlcx20253187, gzlcx20243105).

Conflict of interest

The authors declare that they have no conflict of interest.

Dates

Received 11 September 2025; Revised 30 October 2025; Accepted 29 December 2025; Published online 29 April 2026

References

[1] Zhu Q, Wang L, Guo Y, Liao C, Li F. 2016. Applying LCC compensation network to dynamic wireless EV charging system. *IEEE Transactions on Industrial Electronics* 63(10):6557–6567

[2] Sagar A, Kashyap A, Nasab MA, Padmanaban S, Bertoluzzo M, et al. 2023. A comprehensive review of the recent development of wireless power transfer technologies for electric vehicle charging systems. *IEEE Access* 11:83703–83751

[3] Yan Z, Song B, Zhang Y, Zhang K, Mao Z, et al. 2019. A rotation-free wireless power transfer system with stable output power and efficiency for autonomous underwater vehicles. *IEEE Transactions on Power Electronics* 34(5):4005–4008

[4] Yang L, Zhang Y, Li X, Jian J, Wang Z, et al. 2021. Analysis and design of four-plate capacitive wireless power transfer system for undersea applications. *CES Transactions on Electrical Machines and Systems* 5(3):202–211

[5] Campi T, Cruciani S, Maradei F, Montalto A, Musumeci F, et al. 2021. Centralized high power supply system for implanted medical devices using wireless power transfer technology. *IEEE Transactions on Medical Robotics and Bionics* 3(4):992–1001

[6] Agarwal K, Jegadeesan R, Guo YX, Thakor NV. 2017. Wireless power transfer strategies for implantable bioelectronics. *IEEE Reviews in Biomedical Engineering* 10:136–161

[7] Fu M, Zhang T, Zhu X, Luk PC, Ma C. 2016. Compensation of cross coupling in multiple-receiver wireless power transfer systems. *IEEE Transactions on Industrial Informatics* 12(2):474–482

[8] Huang Y, Liu C, Zhou Y, Xiao Y, Liu S. 2019. Power allocation for dynamic dual-pickup wireless charging system of electric vehicle. *IEEE Transactions on Magnetics* 55(7):8600106

[9] Cheng C, Li W, Zhou Z, Deng Z, Mi C. 2020. A load-independent wireless power transfer system with multiple constant voltage outputs. *IEEE Transactions on Power Electronics* 35(4):3328–3331

[10] Li J, Qin R, Sun J, Costinett D. 2022. Systematic design of a 100-W 6.78-MHz wireless charging station covering multiple devices and a large charging area. *IEEE Transactions on Power Electronics* 37(4):4877–4889

[11] Zhang X, Liu F, Mei T. 2021. Multifrequency phase-shifted control for multiphase multiload MCR WPT system to achieve targeted power distribution and high misalignment tolerance. *IEEE Transactions on Power Electronics* 36(1):991–1003

[12] Huang Y, Liu C, Xiao Y, Liu S. 2020. Separate power allocation and control method based on multiple power channels for wireless power transfer. *IEEE Transactions on Power Electronics* 35(9):9046–9056

[13] Wang NX, Wang HW, Mei J, Mohammadi S, Moon J, et al. 2021. Robust 3-D wireless power transfer system based on rotating fields for multi-user charging. *IEEE Transactions on Energy Conversion* 36(2):693–702

[14] Neath MJ, Swain AK, Madawala UK, Thrimawithana DJ. 2014. An optimal PID controller for a bidirectional inductive power transfer system using multiobjective genetic algorithm. *IEEE Transactions on Power Electronics* 29(3):1523–1531

[15] Yang Y, Zhong W, Kiratipongvoot S, Tan SC, Hui SYR. 2018. Dynamic improvement of series–series compensated wireless power transfer systems using discrete sliding mode control. *IEEE Transactions on Power Electronics* 33(7):6351–6360

[16] Shi W, Deng J, Wang Z, Cheng X. 2018. The start-up dynamic analysis and one cycle control-PD control combined strategy for primary-side controlled wireless power transfer system. *IEEE Access* 6:14439–14450

[17] Li Y, Hu J, Li X, Chen F, Xu Q, et al. 2020. Analysis, design, and experimental verification of a mixed high-order compensations-based WPT system with constant current outputs for driving multistring LEDs. *IEEE Transactions on Industrial Electronics* 67(1):203–213

[18] Li Y, Hu J, Li X, Cheng KE. 2019. A flexible load-independent multi-output wireless power transfer system based on cascaded double T-resonant circuits: analysis, design and experimental verification. *IEEE Transactions on Circuits and Systems I: Regular Papers* 66(7):2803–2812

[19] Luo B, Ma D, Han W, Liu J. 2022. Extensible low-profile coplanar wireless power transfer system for multiload applications with load-independence constant current output. *IEEE Transactions on Industrial Electronics* 69(11):11187–11197